Numerical analysis of the fluid-solid interactions during steady and oscillatory flows of non-Newtonian fluids through deformable porous media

Antonio Rodríguez de Castro[a,*], *Morgan Chabanon*[b], *Benoit Goyeau*[b]

[a] *I2M, Arts et Métiers Institute of Technology, CNRS, Esplanade des Arts et Métiers, 33405 Talence Cedex, France*
[b] *Laboratoire EM2C, UPR CNRS 288, Centrale-Supélec, Université Paris-Saclay, 3 rue Joliot-Curie, 91190 Gif-sur-Yvette, France*

The flow of non-Newtonian fluids through evolving porous media is involved in important processes including blood flow and remediation of deformable aquifers. However, the effects of a moving solid boundary and the coupling between fluid rheology and solid deformation are still unclear. This study considers the steady and oscillatory flows of a yield stress fluid through a bundle of deformable channels. Simple semi-empirical expressions to predict the relationships between Darcy velocity and pressure gradient as a function of pore sizes, shear-rheology parameters and inlet pressure are developped, based on the results of innovative numerical simulations. The results show that channel deformation reduces the minimum pressure gradient required to induce the flow of a yield stress fluid through a porous medium, which results in lower values of Darcy-scale viscosity. For the considered conditions, macroscopic flow can be accurately predicted without a detailed knowledge of the hydraulic conductances of the deformed pores.

Keywords:
Fluid-solid interaction
Non-Newtonian fluids
Pore-scale simulation
Deformable porous media
Constrained elastic duct
Oscillatory flow

1. Introduction

The study of the mechanical interactions between a non-Newtonian fluid and a deformable solid wall is at the interface between fluid physics and solid mechanics, and is of interest in many applications, especially in the health and geosciences fields (soil remediation). For example, the flow of blood throughout the entire vascular network of arteries, veins and vessels of varying sizes plays a major role in the functioning human body by supplying our cells with oxygen and nutrients. A partial or total blockage (thrombus) in this vascular network due to an atheroma deposit consisting of cholesterol and cellular debris on the walls of the arteries (Abbas Nejad et al., 2018) can lead to atherosclerosis and heart attack or to a stroke. A detailed understanding of blood flow both at the local level and at the level of the capillary network is therefore essential for the development of preventive and therapeutic strategies. Locally, a vein is made up of three envelopes of different thicknesses which play an important role in varying degrees of flexibility and elastic behavior. The blood is brought quickly to the tissues where the exchanges take place through capillary vessels. Depending on the section, the conditions of this transport (pressure, velocity) vary, and the vascular network must show resistance and elasticity (arteries and veins) or thinness and high permeability (vessels and capillaries). In addition, blood is a shear-thinning complex fluid, which exhibits non-Newtonian rheology (Chien, 1970; Pourjafar and

* Corresponding author.
E-mail address:
antonio.rodriguez-de-castro@u-bordeaux.fr
(A. Rodríguezde Castro).
https://doi.org/10.1016/j.cherd.2023.03.004

Sadeghy, 2017; Lopes et al., 2020; Ling et al., 2021). Its unsteady circulation through the vascular tree is pulsatile. This situation therefore raises the question of how to accurately represent the interactions between a complex fluid and a deformable capillary. The interest of this research is equally relevant to "in situ" remediation of polluted deformable aquifers, in which the use of complex displacement fluids makes it possible to increase the efficiency of the treatment as compared to waterflooding (Kovscek and Bertin, 2003, Longpré-Girard et al., 2016).

Fluid-structure interactions in elastic tubes have been widely studied, primarily motivated by biofluids in arteries and the lungs (Pedley, 1980; Grotberg, 1994; Grotberg and Jensen, 2004; Heil and Hatzel, 2011; Kizilova et al., 2012). Morgan and Parker (1989) developed a mathematical model of flow of a Newtonian fluid through a collapsible tube and Whitaker et al. (2010) theoretically derived analytical expressions describing oscillatory flow of Newtonian fluids in elastic-walled tubes. However, accounting for the non-Newtonian nature of the fluid in these systems remains an important challenge (Fung, 2013). Recently, interesting developments have been made motivated by the description of non-Newtonian fluids in microfluidic devices, where the polymeric walls are compliant (Raj and Sen, 2016; Raj et al., 2018, Boyko et al., 2017; Anand et al., 2019; Anand and Christov, 2021). Notably, Anand et al. (2019) considered the flow of a non-Newtonian fluid with power-law shear rheology through a rectangular channel whose top wall was linearly elastic and compliant. Two cases were considered for the structure problem, either the Kirchhoff–Love theory of thin plates or the Reissner-Mindlin first-order shear deformation theory. Using lubrication theory, they derived an expression relating the flow rate to the pressure gradient in the form of first order ordinary differential equations for the two cases for low values of Reynolds number Re. They showed that the deformation of the plate is driven solely by the hydrodynamic pressure, i.e., the fluid rheology does not directly affect the displacement profile. Then, they compared the predictions of their model to direct numerical simulations, showing excellent agreement in the linear deformation regimes. The same approach was subsequently extended to the flow of a power-law fluid in a slender elastic tube (Anand and Christov, 2021), showing that pressure drop is non-linearly related to the flow rate, even for Newtonian fluids. Vedeneev (2020) analyzed the possible steady states of an elastic tube made of an incompressible hyperelastic Gent material conveying a power-law fluid. The author concluded that, for sufficiently small fluid velocities, localized swelling or necking solutions for a tube that is infinitely long in both directions do not exist. Nevertheless, such solutions exist if the tube is semi-infinite, without the possibility of multiple neckings or swellings. For finite-length tubes, several solitary wave, periodic wave, and monotonic solutions exist. Based on lubrication approximation, Venkatesh et al. (2022) modelled the transient flow of simplified Phan–Thien–Tanner fluids and power-law fluids peeling two Hookean sheets at low values of Re. Their numerical simulations showed that the peeling time for the shear-thinning fluid is much smaller than the equivalent Newtonian fluid. Moreover, Boyko and Christov (2023) recently studied the flow of an Oldroyd-B fluid in a deformable channel with a compliant top wall. They theoretically modeled the effects of viscoelasticity on deformation profile and flow rate-pressure drop relationships using the Kirchhoff–Love plate-bending theory. They showed that while the channel's compliance increases the deformation, the fluid's viscoelasticity decreases it. However, both the compliance of the deforming top wall and the viscoelasticity of the fluid decrease the pressure drop.

Given the complexity of the flow of a non-Newtonian fluid in a deformable capillary, it is currently impossible to solve such a flow in an entire network. This challenge related to the separation of scales between the local flow and the macroscopic network is comparable to an upscaling problem in transport in porous media (Quintard and Whitaker, 1993; Bergamasco et al., 2015). Therefore, theoretical and numerical tools developed in porous media literature can be applied (Peyrounette et al., 2018), e.g., pore network modeling (Rodríguezde Castro and Goyeau, 2021) and volume averaging method (Whitaker, 1999). While the first approach represents the porous medium as a network of pores connected by capillaries with equivalent hydraulic resistances, the second is a homogenization method allowing to develop a continuous equivalent representation at the scale of the network. The complementarity of these approaches enables the calculation of quantities such as the permeability of the network as a function of the non-Newtonian properties of the fluid, the mechanical properties of the channels, and the structure of the network.

The present study focuses on developing a model for the stationary and oscillatory flow of a yield stress fluid through a model deformable porous medium consisting of a bundle of elastic channels. The main stumbling block remains the existing coupling between the state of deformation of the channels and the distribution of viscosities resulting from the non-Newtonian behavior of the fluid. In other words, the viscosity of the complex fluid in a channel depends on the aperture of the channel, which varies during deformation. However, the distribution of strains will, in turn, depend on the pressure distribution generated by the local viscosity values. First, a set of numerical simulations of the flow of a yield stress fluid through an individual deformable channel will be presented. These simulations were performed using the finite element method with a moving grid to take into account the deformation of the walls. The results of these first simulations will be subsequently used to analyze the relationships between fluid pressure and flow rate through an individual element of a pore network, depending on the mechanical properties and dimensions of the solid wall. Then, another set of direct numerical flow simulations will be presented, which was performed on a simple porous medium consisting of a bundle of parallel unconnected channels. A semi-empirical model will be proposed to represent the relationships between Darcy viscosity and velocity based on the results of such simulations. This represents the first step toward the development of a more general model capable of predicting steady flows of complex fluids in real 3D porous media. In a second time, oscillating flows of yield stress fluids will be also tackled in this work. To do so, a sinusoidally varying inlet pressure will be imposed in the simulations and the results of the flow through a deformable and a rigid bundle of channels will be compared. As in the stationary case, the analysis of the results of oscillatory flow simulations will allow for the development of semi-empirical expressions relating Darcy-scale flow rate and viscosity to the applied pressure gradient.

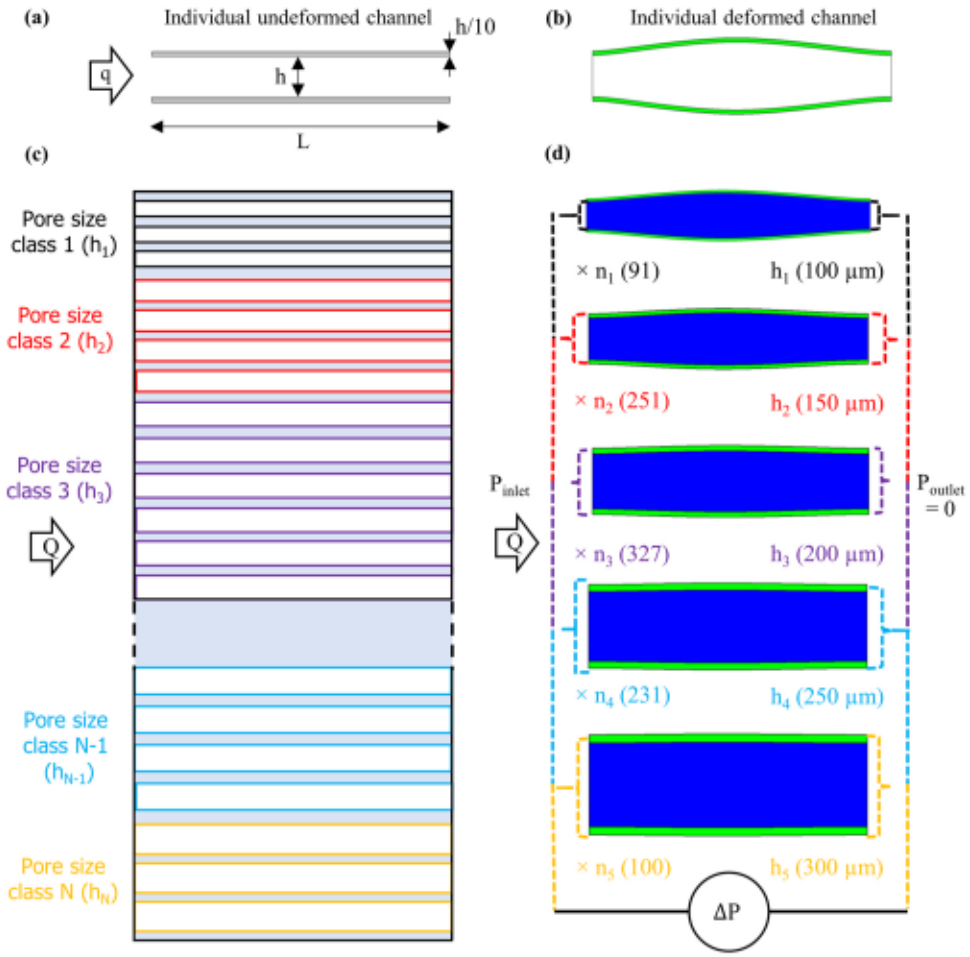

Fig. 1 – (a) Individual undeformed channel considered in the present simulations. q is the individual flow rate through a channel of aperture h given by Eq. (2). (b) Individual channel at the deformed state. The channel is constrained at the inlet and the outlet. (c) Schematic view of a porous medium consisting of a generic bundle of unconnected parallel rectangular channels of same length and infinite depth (depth is perpendicular to the represented view). The channel sizes are distributed among N different classes. Q is the total flow rate through the porous medium given by Eq. (12). The channels are represented at their undeformed state (d) Bundle of elastically deformable channels considered in the present simulations represented at their deformed state. ΔP is the pressure drop between the inlet and the outlet, P_{inlet} and P_{outlet} are the inlet and outlet pressures.

2. Modelling aspects

The following subsections present the numerical procedures used to simulate the steady and oscillatory flows of Herschel-Bulkley fluids through individual deformable channels and a bundle of rectangular channels representing a model porous medium.

2.1. *Geometries*

Given its transversal nature, this research was approached in a general way, using a standard geometry consisting of rectangular pores of infinite depth. First, the incompressible flow of a Herschel-Bulkley fluid through an individual 2D channel of length L and aperture h was studied, as illustrated in Fig. 1(a,b). These channels are constrained at their inlet and their outlet (no displacement of the wall is allowed at these locations). The width of the solid walls of the channel was h/10. The solid was assumed to be an isotropic linear elastic material. Its Young's modulus E was varied depending on the considered simulation, while its Poisson's ratio ν and its density ρ_s were set to 0.4 and 1100 kg/m^3, respectively, in all the numerical experiments. The tested values of E ranged from 3×10^5 Pa to 1×10^8 Pa, which corresponded to different types of real-world materials. For example, typical values of E for polydimethylsiloxane (PDMS), a polymeric gel widely used in microfabrication (McDonald and Whitesides, 2002; Anand et al., 2019) are close to 1×10^6 Pa (Boyko et al., 2017). Regarding geo and biomaterials, common values of E for layered sand aquifers are close to 1×10^7 Pa (Kim and Parizek, 2005), while wood develops values of E of approximately 1×10^8 Pa (Alves et al. 2013). E falls typically in the range 1×10^5 to 1×10^6 Pa for iliac arteries and abdominal aorta (Canic et al., 2005). The values of ν and ρ used in the present simulations are commonly encountered in blood vessels (van de Vosse, 2013). In a second step, a bundle composed of 1000 straight ducts of 5 different sizes was considered, as displayed in Fig. 1(c,d). The aperture classes h_i of the ducts followed a discrete normal distribution: 91 ducts of 100 µm, 251 ducts of 150 µm, 327 ducts of 200 µm, 231 ducts of 250 µm and 100 ducts of 300 µm aperture. The total width of the rigid bundle W was 0.5 m, its permeability $K = 1.64 \times 10^{-9}$ m^2, and

its porosity $\varepsilon = 0.40$. These values also correspond to the reference values of the deformable bundle when subjected to zero inlet pressure. It should be noted that the chosen values of K and ε fall within the range of those commonly presented by porous scaffolds for bone tissue engineering (Innocentini et al., 2010) in biomedical applications and by fractured rocks, sand packs and gravel (Bear, 1972) in geophysics.

Since the objective was to examine the effects of the coupling between fluid rheology and solid deformation on the flow of a yield stress fluid through a porous media, the present study was carried out considering 2D bundles of deformable channels, with different sizes. This model 2D geometry allowed to qualitatively assess such effects and to develop expressions to predict the apparent viscosity in the porous medium and the relationships between pressure conditions and flow rate. This choice was further motivated by the fact that accurate numerical simulations are more tractable, and their results can be more easily and more clearly interpreted in the 2D case. It should also be noted that the 2D channels are not connected, which should result in similar tortuosity of the flow streamlines for both the 2D and the 3D cases. Moreover, a thorough analysis of 2D and three-dimensional (3D) flows of yield stress fluids in porous media (Talon and Bauer, 2013; Bauer et al., 2019) showed that the same flow regimes are observed in both cases. However, considering 3D geometries implies the addition of two non-slip conditions in the depth direction, which is expected to affect the computed physical quantities. Therefore, 3D geometries must be used to obtain accurate predictions in many real applications.

2.2. Fluid

Herschel-Bulkley's law was used to describe the steady-state shear rheology of the yield stress fluids considered in the present work (Eq. 1):

$$\begin{Bmatrix} \tau = \tau_0 + k\dot{\gamma}^n \text{ for } \tau \geq \tau_0 \\ \dot{\gamma} = 0 \text{ for } \tau \leq \tau_0 \end{Bmatrix} \tag{1}$$

In this model, τ_0 is the yield stress, k is the consistency and n is the flow index of the fluid. τ and γ are the shear stress and shear rate, respectively. Hershel-Bulkley model is commonly used to describe the shear rheology of blood (Scott Blair and Spanner, 1974; Sankar and Hemalatha, 2007; Sankar and Lee, 2009) and the one of a great number of chemicals injected during soil remediation operations, e.g., foams (Omirbekov et al., 2020) or concentrated polymer solutions (Rodríguezde Castro, 2019). In the reference case of the steady flow of a Herschel-Bulkley fluid through a straight rigid channel of constant aperture h_i and infinite depth, the relationship between the flow rate per unit depth q and the applied pressure gradient ∇P is expressed as (Skelland, 1967; Chhabra and Richardson, 2008, Ferrás et al., 2012):

$$q(\nabla P, h_i) = \begin{cases} 2\left[\frac{n}{n+1}\left(\frac{\nabla P}{k}\right)^{1/n}\left[\frac{h_i h}{2}\left(\frac{h_i}{2}-\frac{h_0}{2}\right)^{1+1/n} - \frac{n\left(\frac{h_i}{2}-\frac{h_0}{2}\right)^{2+\frac{1}{n}}}{1+2n}\right]\right] & \text{for } h_i \geq h_0 \\ 0 \quad \text{for} \quad h_i \leq h_0 \end{cases} \tag{2}$$

with $h_0 = \frac{2\tau_0}{\nabla P}$.

2.3. Conservation equations

The pressure p, solid displacement $\mathbf{d_s}$ and fluid velocity $\mathbf{u_f}$ fields were computed in each simulation by solving the following equations:

$$\rho\frac{\partial \mathbf{u_f}}{\partial t} + \rho(\mathbf{u_f}\cdot\nabla)\mathbf{u_f} = \nabla\cdot[-pI + \mu(\nabla\mathbf{u_f} + (\nabla\mathbf{u_f})^T)] \tag{3}$$

$$\nabla\cdot\mathbf{u_f} = 0 \tag{4}$$

$$\rho_s\frac{\partial^2\mathbf{d_s}}{\partial t^2} = \nabla\cdot\boldsymbol{\sigma} \tag{5}$$

with Eq. (5) being Cauchy momentum equation, ρ being the density of the fluid and $\boldsymbol{\sigma}$ being Cauchy stress tensor:

$$\boldsymbol{\sigma} = J^{-1}\mathbf{F}\mathbf{S}\mathbf{F}^T \tag{6}$$

$$\mathbf{F} = (I + \nabla\mathbf{d_s}) \tag{7}$$

S is the second Piola-Kirchhoff stress tensor, **F** is the deformation gradient tensor and $J = \det(\mathbf{F})$.

$$\mathbf{S} = \mathbf{C}:\boldsymbol{\epsilon} \tag{8}$$

$$\boldsymbol{\epsilon} = \frac{1}{2}[(\nabla\mathbf{d_s})^T + \nabla\mathbf{d_s} + (\nabla\mathbf{d_s})^T\nabla\mathbf{d_s}] \tag{9}$$

with **C** being the fourth order elasticity tensor, : being the double-dot tensor product and $\boldsymbol{\epsilon}$ being the displacement gradient tensor. **C** is given as $C_{ijkl} = \frac{\nu E}{(1+\nu)(1-2\nu)}\delta_{ij}\delta_{kl} + \frac{E}{2(1+\nu)}(\delta_{ik}\delta_{jl} + \delta_{il}\delta_{jk})$.

To implement numerically the yield-stress fluid behaviour of Eq. (1), the viscosity was set in the model as:

$$\mu = \min\left[\mu_{max}, \left(k\dot{\gamma}^{n-1} + \frac{\tau_0}{\dot{\gamma}}\right)\right] \tag{10}$$

where μ_{max} corresponds to the maximum viscosity exhibited by the fluid at the lowest shear rates. It should be noted that, while viscosity tends to infinity in Herschel-Bulkley model (Eq. 1) when shear rate tends to zero, most real shear-thinning fluids develop a maximum viscosity plateau ($\mu = \mu_{max}$). The viscosity plateau value is very high in the case of yield stress fluids. In the current work, the shear-rheology parameters of the investigated yield stress fluid were $\tau_0 = 10$ Pa, $k = 1$ Pa s^n, $n = 0.5$ and $\mu_{max} = 10{,}000$ Pa s. The chosen value of μ_{max} corresponded to shear rates lower than $\dot{\gamma} = 10^{-3}$ s^{-1} and the values of τ_0, k and n were close to those of concentrated xanthan gum aqueous solutions exhibiting a yield stress (Rodríguezde Castro et al., 2021). $\dot{\gamma}$ is the generalized shear rate computed using Einstein's summation convention: $\dot{\gamma} = \sqrt{2\Delta_{i,j}\Delta_{i,j}}$, with Δ being the strain rate tensor.

The outlet pressure and the pressure on the external faces of the solid walls were set to 0. The horizontal displacement (x-direction) of the external faces of the solid walls was prescribed to 0 (van de Vosse, 2013; Canic et al., 2015; Gomez et al., 2017) and the inlet and outlet boundaries of the fluid domain were fixed. The solid walls situated at $x = 0$ (inlet) and $x = L$ (outlet) were also fixed ($\mathbf{d_s} = \mathbf{0}$) (Van de Vosse, 2013; Chakraborty and Prakash, 2015; Gomez et al., 2017). The kinematical conditions in the solid-fluid boundary were continuation of velocity in the vertical and horizonal directions:

$$\mathbf{u_f} = \frac{\partial\mathbf{d_s}}{\partial t}$$

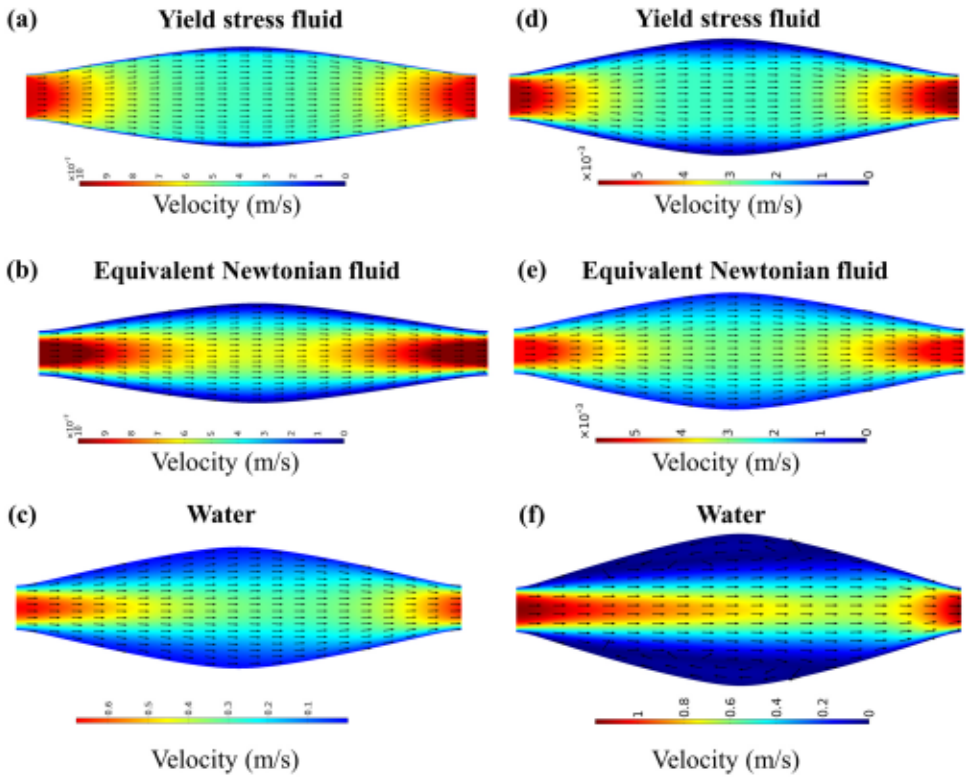

Fig. 2 – Velocity map in a single rectangular duct of infinite depth, 1 millimeter length, 100 μm aperture and E = 10^6 Pa under an inlet pressure P_{inlet} of (a,c,d) 160 Pa and (b,d,f) 320 Pa. The different cases corresponding to the yield stress fluid, the equivalent Newtonian fluid and water are represented. The shear viscosities of the equivalent Newtonian fluids were 490 Pa s for the P_{inlet} = 160 Pa and 0.21 Pa s for P_{inlet} = 320 Pa. Color map represents velocity magnitude and black arrows represent the directions and senses of velocity vectors.

The dynamical boundary condition at the fluid-solid interface is given by:

$$\boldsymbol{\sigma}\cdot\mathbf{n} = \boldsymbol{\Gamma}\cdot\mathbf{n}$$

$$\text{with}\boldsymbol{\Gamma} = [-p\mathbf{I} + \mu(\nabla\mathbf{u}_f + (\nabla\mathbf{u}_f)^T)]$$

where p denotes pressure, I is the identity matrix, μ is the local dynamic viscosity of the fluid and **n** is the normal direction vector.

2.4. *Numerical simulations*

The fluid-structure interaction module of COMSOL Multiphysics version 5.3. (2017) was used to solve the flow problems under consideration. An Arbitrary Lagrangian-Eulerian (ALE) technique was used to manage the dynamics of the changing geometry and the displacement of the boundaries by means of a moving grid. New mesh coordinates were computed within the channel region based on the movement of the solid boundaries and mesh smoothing. In the flow portion of the local model, mass and momentum conservation equations were solved using such moving coordinates. In contrast, the structural mechanics part of the local model was solved by using a classical fixed coordinate system. The computational domain was meshed using triangular elements. Mesh-independent converged numerical solutions were determined through a sensitivity analysis of the solution to the number of elements. The inlet (left boundary) flow rate per unit depth q was used as the basis for comparison in the sensitivity analysis. The computed values of q were normalized by the flow rate obtained with the finest mesh. A mesh sensitivity analysis on the rectangular duct displayed in Fig. 2 is presented for P_{inlet} = 120 Pa and P_{inlet} = 210 Pa in Fig. S1 of the supplementary material. This figure shows that mesh-independence is achieved after about 10k elements with a tolerance of 5% deviation from the reference solution. Increasing the number of grid blocks 7 times, from a mesh of ~17k to ~120k elements, leads to a relative error on the flow rate of 3%. Thus, the mesh adopted in the test case had ~17k elements as a trade-off between acceptable accuracy and computation time. The average skewness-based quality of the generated mesh was 0.9384, where 1 represents a perfectly regular element, in the chosen quality measure, and 0 represents a degenerated element.

2.4.1. *Steady flow simulations*

A first set of simulations was conducted in which the steady flow of a yield stress fluid through a single deformable channel was simulated. In each simulation, N different values of the inlet pressure P_{inlet} were imposed, and the corresponding values of the flow rate per unit depth q were computed by integrating the x-component of the fluid velocity vectors along the inlet boundary of the fluid domain. By doing so, a set of $(\nabla P_j, q_j)$ numerical datapoints were obtained, with j = 1…N and $\nabla P_j = \frac{\Delta P_j}{L}$.

As reported by Lavrov (2013), it is sometimes convenient to replace the real channel with an "equivalent" channel with fixed parallel walls when incorporating microscopic fluid flow into higher-level models. In this regard, the equivalent aperture h_{eq} of the deformed channel (di Federico, 1997; 1998; Gomez et al., 2017) is defined in this study as the aperture of a rigid channel with parallel walls that would produce the same flow rate under a given applied pressure

gradient as the real deformable channel. From Eq. (2), the following expression can be written to express q in the 2D deformable channels:

$$q_j(\nabla P_j, h_{eq,j}) = \begin{cases} 2\left[\frac{n}{n+1}\left(\frac{\nabla P_j}{k}\right)^{1/n}\left[\frac{h_{eq,j}}{2}\left(\frac{h_{eq,j}}{2}-\frac{h_0}{2}\right)^{1+1/n}-\frac{n\left(\frac{h_{eq,j}}{2}-\frac{h_0}{2}\right)^{2+\frac{1}{n}}}{1+2n}\right]\right] & \text{for} \quad h_{eq,j} \geq h_0 \\ 0 \quad \text{for} \quad h_{eq} \leq h_0 \end{cases} \tag{11}$$

with $h_0 = \frac{2\tau_0}{\nabla P_j}$. Eq. (11) was numerically solved by using the differential evolution method for each numerically computed (∇P_j, q_j) datum to obtain the values of $h_{eq,j}$.

Different values of E were used depending on the simulation so as to investigate the effects of this mechanical property on the magnitude of the maximum wall displacement and h_{eq}. Furthermore, the sensitivity of the maximum wall displacement to h and L was also evaluated. All the considered values of P_{inlet} were increased proportionally to the increase in L in order to keep the same range of ∇P in all cases.

Macroscopic flow rate-pressure drop relationships are required to predict single-phase flow of non-Newtonian fluids in porous media. To develop such relationships, an appropriate representation of the porous medium is needed that captures its main macroscopic and microscopic hydraulic properties. Savins (1969) reviewed the methods for correlating the apparent viscosity of the fluid in the porous medium with viscosimetric measurements. Four main types of methods exist: the methods based on the capillary model-hydraulic radius concept, the generalized upscaling methods allowing for the extension of Darcy's law to non-Newtonian fluids without invoking the use of a particular rheological model, the methods involving the application of dimensional analysis and other correlation methods. A widely used method consists in representing the medium by a bundle of parallel regular-shaped pores with the same overall resistance to flow as the porous medium replaced. This idealized geometry is known as the bundle-of-capillaries model, and has been used to describe the flow of non-Newtonian fluids in the past (López et al., 2003; Sochi, 2010; Shende et al., 2021).

In a second set of numerical experiments, the steady flow of a yield stress fluid through the model porous medium represented in Fig. 1(d) was simulated, contrarily to the first set of simulations in which the flow through a single channel was considered. As can be observed in Fig. 1(d), the model porous medium was a bundle of deformable ducts with different apertures. The total flow rate through the bundle per unit depth Q_j under a given pressure gradient ∇P_j was computed as the frequency-weighted sum of the flow rates through the ducts of each aperture class:

$$Q_j(\nabla P_j) = \sum_{i=1}^{5} n_i q(\nabla P_j, h_i) \tag{12}$$

with n_i being the number of channels of aperture class h_i. For each simulation, $Q_j(\nabla P_j)$ were also computed assuming a rigid bundle with the same distribution of the channel apertures as the deformable bundle by using Eq. (2) and (12). For the sake of comparison with a Newtonian fluid, the flow of water (constant dynamic viscosity taken as 10^{-3} Pa s) was also simulated for the whole range of boundary conditions investigated in the current simulations. In some particular cases that will be described below, the flow of an equivalent Newtonian fluid producing the same flow rate as the yield stress fluid for a given inlet pressure was also simulated. Therefore, the viscosity of the Newtonian equivalent was chosen so that Re of its flow was identical to the one of the flow of the yield stress fluid. Re was defined by using h_{eq} as characteristic length and the effective viscosity μ_{eff} provided by plane Poiseuille flow equation in a straight channel of aperture h_{eq} as characteristic viscosity of the yield stress fluid, i.e., $Re = \frac{\rho u h_{eq}}{\mu_{eff}}$.

Darcy's law was used in the past to describe the flow through a porous medium with deformable pores. In this respect, Rosti et al. (2020) developed a Darcy-like relation between flow rate and pressure difference for the flow of a Newtonian fluid through a model deformable porous medium in which the pores were considered to be elastic channels. For the single-phase creeping flow of incompressible fluids through a 2D porous medium at Darcy scale, Darcy viscosity μ_{pm}, also known as apparent viscosity, can be calculated from Darcy's law as:

$$\mu_{pm} = -\frac{KW}{Q}\nabla P = -\frac{K}{u}\nabla P \tag{13}$$

with K being the intrinsic permeability of the porous medium, W being its total width, Q the injection flow rate per unit depth, u (= Q/W) Darcy velocity and ∇P the pressure gradient. μ_{pm} was used to characterize the apparent viscosity exhibited by the non-Newtonian fluid during its flow through the porous media. It is worth highlighting that μ_{pm} is a function of u for a non-Newtonian fluid. It should also be noted that the contributions of both inertial and viscous pressure drops are encompassed in ∇P for the calculation of μ_{pm} (Tosco et al., 2013). In the presence of inertial pressure drops, μ_{pm} is defined as the expression that must replace the viscosity in the Darcy law to result in the same pressure drop predicted by the Darcy–Forchheimer equation (Forchheimer, 1901). By using μ_{pm}, the Darcy–Forchheimer equation can be written in a form similar to standard Darcy law with only one term expressing the (fictitious) linear dependence of ∇P on the flow rate. Darcy-Forchheimer equation was used in preceding works to model the flow of shear-thinning fluids in porous media and rough-walled rock fractures (Tosco et al., 2013; Rodríguezde Castro and Radilla, 2016; Rodríguezde Castro and Radilla, 2017a). However, given the high values of shear viscosity exhibited by the considered yield stress fluid during its flow through the bundle of channels, inertial pressure drops were neglected in the calculation of μ_{pm}. For example, if the 100 μm channel with $E = 3 \times 10^5$ Pa is considered, the values of Re developed by water ranged from ~ 7.3×10^1 to ~ 1.4×10^2 in the present simulations, while the values of Re developed by the yield stress fluid and its Newtonian equivalent ranged from ~ 2.4×10^{-8} to ~ 1.1×10^2 for the same range of ∇P. Also, it is reminded that the

permeability of the deformable bundle is expected to increase when the P_{inlet} is increased because of the elastic deformation of the channel walls. In the present study, K used in Eq. (13) is taken as a reference value corresponding to the intrinsic permeability of the undeformed bundle (i.e., when P_{inlet} is equal to zero), which is the same as the permeability of the rigid bundle. The value of μ_{pm} corresponding to each (∇P_j, u_j) datapoint, named $\mu_{pm,j}$, was calculated.

Knowing the value of $\mu_{pm,j}$, the apparent shear rate in the porous medium $\dot{\gamma}_{pm,j}$ was computed using the constitutive equation of the fluid (Eq. 1), by numerically solving the next equation:

$$\mu_{pm,j} = k\dot{\gamma}_{pm,j}^{n-1} + \frac{\tau_0}{\dot{\gamma}_{pm,j}} \tag{14}$$

$\dot{\gamma}_{pm,j}$ corresponds to the wall shear rate in the average pore throat diameter (Chauveteau and Zaitoun, 1981; Chauveteau, 1982; Sheng, 2011). In the case of a bundle of 2D channels, $\dot{\gamma}_{pm,j}$ can be defined as six times the average pore velocity 6 u/ε divided by a characteristic length of the microscopic flow (Pipe et al., 2008; Rodríguezde Castro and Radilla 2017b). The characteristic length of the microscopic flow is often taken as $\frac{h_{hyd}}{\alpha}$ where h_{hyd} is the hydraulic aperture of the bundle of non-uniform channels. h_{hyd}corresponds to the aperture of the channels in a bundle of uniform channels generating the same pressure drop as the considered bundle of non-uniform channels when a Newtonian fluid is injected at the same flow rate. From Darcy's equation and Poiseuille's law, the following expression can be deduced:

$$h_{hyd} = \frac{\sqrt{12K}}{\varepsilon} \tag{15}$$

α is an empirical shift factor known to be a function of both the bulk rheology of the fluid and the porous medium [Chauveteau, 1982; Sorbie et al., 1989; López et al., 2003; Comba et al., 2011; Rodríguezde Castro and Agnaou, 2019]. α is introduced in the definition of $\dot{\gamma}_{pm,j}$ in order to fit Darcy-scale viscosity μ_{pm} to the shear viscosity vs. shear rate measurements obtained with a rheometer. From the preceding remarks, the following expressions of $\dot{\gamma}_{pm,j}$ and α_j can be written:

$$\dot{\gamma}_{pm,j} = \alpha_j \frac{6\frac{u_j}{\varepsilon}}{h_{hyd}} = \alpha_j \frac{\sqrt{3}\,u_j}{\sqrt{K\varepsilon}} \tag{16}$$

$$\alpha_j = \dot{\gamma}_{pm,j} \frac{\sqrt{K\varepsilon}}{\sqrt{3}\,u_j} \tag{17}$$

While α was independent of u for Newtonian and power-law fluids, previous works showed that α is a function of u for the flow of a yield stress fluid in a porous medium (Rodríguezde Castro and Agnaou, 2019; Rodríguezde Castro, 2019). This explains the subscript j of α_j used in Eq. (16) and Eq. (17). Although α is known to decrease when u is increased during the injection of yield stress fluids through rigid porous media, this is not necessarily the case when the pores are deformable. It is an additional objective of the present study to identify the effects of deformation on the relationships between α_j and u. This was achieved by applying Eq. (17) to the results of the present simulations through the rigid and the deformable bundles of channels.

2.4.2. *Transient flow simulations*

The oscillatory flow of a Herschel-Bulkley fluid through the bundles of rigid or deformable channels described in subsection 2.1 was also considered. In this case, the time dependence of P_{inlet} was described by a sinusoidal function of the form:

$$P_{inlet}(t) = \bar{P}\left(1 + 0.25\sin\frac{2\pi}{T}t\right)$$

with $\bar{P}$ being the time averaged inlet pressure and T the period of the oscillation. Different sets of simulations were performed by setting $\bar{P}$ to 250 Pa, 300 Pa, 400 Pa, 700 Pa and 1000 Pa, respectively, while keeping T equal to 1 s. E was taken as 10^7 Pa in all oscillatory flow simulations. The unsteady flow was simulated over two oscillation periods. In each time dependent simulation, the results of a steady state simulation using $P_{inlet} = \bar{P}$ were used as initial guess of the dependent variables. Prior to the calculation of the flow rate through the whole porous medium, the individual contributions of single channels of different aperture were computed. Moreover, the time evolution of h_{eq} was monitored for each aperture class for the different values of $\bar{P}$.

An important remark is that the oscillatory flow rate of a Herschel-Bulkley fluid through a rigid tube cannot be directly calculated by using Eq. (2), because of the unsteady nature of the flow. However, Eq.(2) can be used to predict the time evolution of the flow rate through a rigid channel with reasonable accuracy for long oscillation periods (succession of steady states). For example, the maximum difference obtained when comparing the flow rate computed through DNS and the one provided by Eq.(2) for $\bar{P}$ = 300 Pa and T = 1 s was 6%. In our aim to provide simple analytical expressions to predict this type of flows, the appropriateness of approximating the total flow rate through the rigid bundle as the one provided by Eqs.(2) and (13) was evaluated. Therefore, the flow rate per unit depth in the rigid bundle was calculated as:

$$Q_{rigid}(t) = \sum_{i=1}^{5} n_i q(\nabla P(t), h_i) \tag{18}$$

It should also be noted that the flow rate at the inlet can be different from the flow rate at the outlet during unsteady flow because of solid wall displacement. u was defined at the inlet for the calculations of μ_{pm} in the present work. In the same manner as for the steady flow, the evolution of μ_{pm} over time was determined for each case and the cases of rigid and deformable bundles were compared.

3. Numerical results

3.1. *Numerical validation*

The experimental procedure presented in 2.4 was validated by comparing the results provided by these numerical simulations to the predictions of fluid-structures interaction theory and the results of previous numerical simulations. Given that no results are currently available for the flow of a yield stress fluid in constrained rectangular ducts, the flow of a power-law fluid through a 3D rectangular channel with an elastically deformable wall was simulated. The same fluid, geometry and mechanical properties of the solid as those used in the benchmark simulations of Anand et al. (2019) were considered. To do so, different inlet pressures were tested, and the corresponding flow rates were computed using the procedure described in subsection 2. The computed flow rates were then compared to the results of the preceding authors, obtaining relative differences of 8% or less. Fig. S2 of

the supplementary material provides a comparison between the numerical results of Anand et al. (2019) and the ones provided by the current simulations. It can be deduced that the results provided by the present simulations are in good agreement with those of the preceding authors and with the analytical expressions presented in their work for power-law fluids. It should be mentioned that ANSYS software was used by Anand et al. (2019), while COMSOL was used in the present study. Also, the channels considered by these authors were 3D. Their 3D channels had a single deformable wall (the top wall) with no displacements allowed at its perimeter. In the present simulations, the channels were 2D apart from the 3D simulations conducted for comparison with the work of the preceding authors (Fig. S2). Moreover, Anand et al. (2019) performed a mathematical analysis in which lubrication approximation was assumed. Lubrication approximation states that pressure becomes independent of the position in the depth and width directions, and a "long and thin" flow geometry. The theoretical predictions of these authors were in good agreement with their numerical results.

3.2. *Steady flows of a yield stress fluids in deformable channels*

3.2.1. *Effects of Young's modulus on pressure distribution, velocity maps, equivalent aperture and wall displacement*

The results of the steady flow simulations provided the distribution of velocities within the deformed channel. Some examples are displayed in Fig. 2. The results for the flow of the considered yield stress fluid under two values of P_{inlet} are represented. For comparison, two Newtonian fluids were considered: equivalent Newtonian fluids developing the same effective viscosity as the yield stress fluid for the two considered pressures, and water. As expected, the highest velocities values were obtained for water, which is less viscous than the other fluids, for both values of P_{inlet}. It was observed that whereas the flow velocities are well distributed throughout the channel for the yield stress fluid (Figs. 1a and 1d), this is neither the case for the equivalent Newtonian fluid nor for water. Indeed, most flow is concentrated in the central part of the channel for the Newtonian fluids, with some recirculation zones appearing in the vicinity of the walls for $P_{inlet} = 320$ Pa in the case of water. The fluid develops very low velocities in these recirculation zones. Additional simulations were performed on a rigid channel having a converging-diverging geometry, mimicking the shape of the deformed elastic channels, in order to identify the role of deformation on the generation of recirculation zones. The results of such simulations showed that recirculation zones arise also in a rigid channel for similar values of Re ($\sim$ 100), revealing their inertial nature.

To facilitate the analysis, the wall displacement distribution, the pressure distribution along the x-direction and the horizontal velocity component distribution along the x-direction are shown in Fig. 3. The pressure and horizontal velocity distributions corresponded to the central plane of the channel. The first remark is that wall displacements are higher for water than for the investigated yield stress fluid and its Newtonian equivalent, for both inlet pressures. However, the maximum wall displacement obtained for the yield stress fluid is identical to the one observed with its Newtonian equivalent. This suggests that wall displacement of a given elastic channel is only a function of the effective viscosity of the fluid and the inlet pressure with no significant influence of viscosity distribution within the flow region. In this regard, the mathematical analysis performed by Anand et al. (2019) using lubrication approximation showed that the deformation of a linearly elastic solid wall is coupled to the fluid mechanics only through the hydrodynamic pressure. Indeed, the rheological parameters of the fluid do not explicitly affect the displacement maps. As stated by these authors, although the hydrodynamic pressure depends on the flow profile, which depends in turn on the rheological model, none of this information is required to write down the deflection profiles explicitly.

Fig. 3(b) shows that pressure monotonically decreases with increasing x-coordinate for the yield stress fluid and its Newtonian equivalent, despite channel expansion, which is explained by strong viscous pressure losses. However, the pressure of water decreases in the expanded zone and drastically decreases in the final constriction. It can be deduced that the recirculation zones observed in Fig. 2 arise from the non-monotonic pressure distribution. The initial increase in the pressure of water also explains the higher wall displacements as compared to the case of the yield stress fluid. An interesting feature is that pressure distribution is not identical for the yield stress fluid and its Newtonian Equivalent, showing the influence of local viscosity distribution on pressure drop between the inlet and an intermediate section of the channel. Regarding the velocity distributions displayed in Fig. 3(c,d), one may notice that a low-velocity plateau is developed by the yield stress fluid for the intermediate values of x-coordinate. This corresponded to the zones in which the shear stress of the fluid falls below the yield stress, generating extremely high viscosity values ($\mu \approx \mu_{max}$) and piston-like flow. In contrast, the velocity of the Newtonian fluid decreases throughout the channel until the final constriction is reached (Fig. 3e).

The effects of E on the q vs. ∇P relationship during the flow through a single channel of 100 µm aperture is displayed in Fig. 4(a). The non-linearity is strong, given that the non-linear evolution of μ with $\dot{\gamma}$ (Eq. 10) for the yield stress fluid adds to the geometrical changes induced by the increase in ∇P. Another important feature is the low-q plateau obtained at the lowest ∇P, which reflects that the fluid remains practically stagnant ($\mu = \mu_{max}$) below a critical value of ∇P. This critical value is equal to $\nabla P = \frac{2\tau_0}{h}$ for a rigid duct of aperture h (2×10^5 Pa/m for a 100 µm aperture channel and the investigated yield stress fluid), but decreases significantly as the value of E is decreased. This means that the onset of flow in the deformable channel is lower than the one observed in a rigid channel, despite the identical size of the narrowest section situated at the constrained inlet and outlet positions. This observation is not trivial as it shows that the same pores can be either open or blocked to the flow of a yield stress fluid depending on their elasticity. This is expected to have an impact for example in soil remediation applications involving the use of yield stress fluids as blocking agents to divert the flow of subsequent waterflooding operations. Indeed, the success of such operations could be jeopardized in the presence of important soil deformation.

Fig. 4(b) shows the dependence of h_{eq} on ∇P relationship for the flow of a Herschel-Bulkley through a single channel of 100 µm aperture. These results are consistent with Fig. 4(a), and h_{eq} increases with ∇P above a critical value of ∇P for the yield stress fluid. These h_{eq} vs. ∇P relationships are expected to be useful when implementing a pore network modelling approach in deformable porous media allowing for the

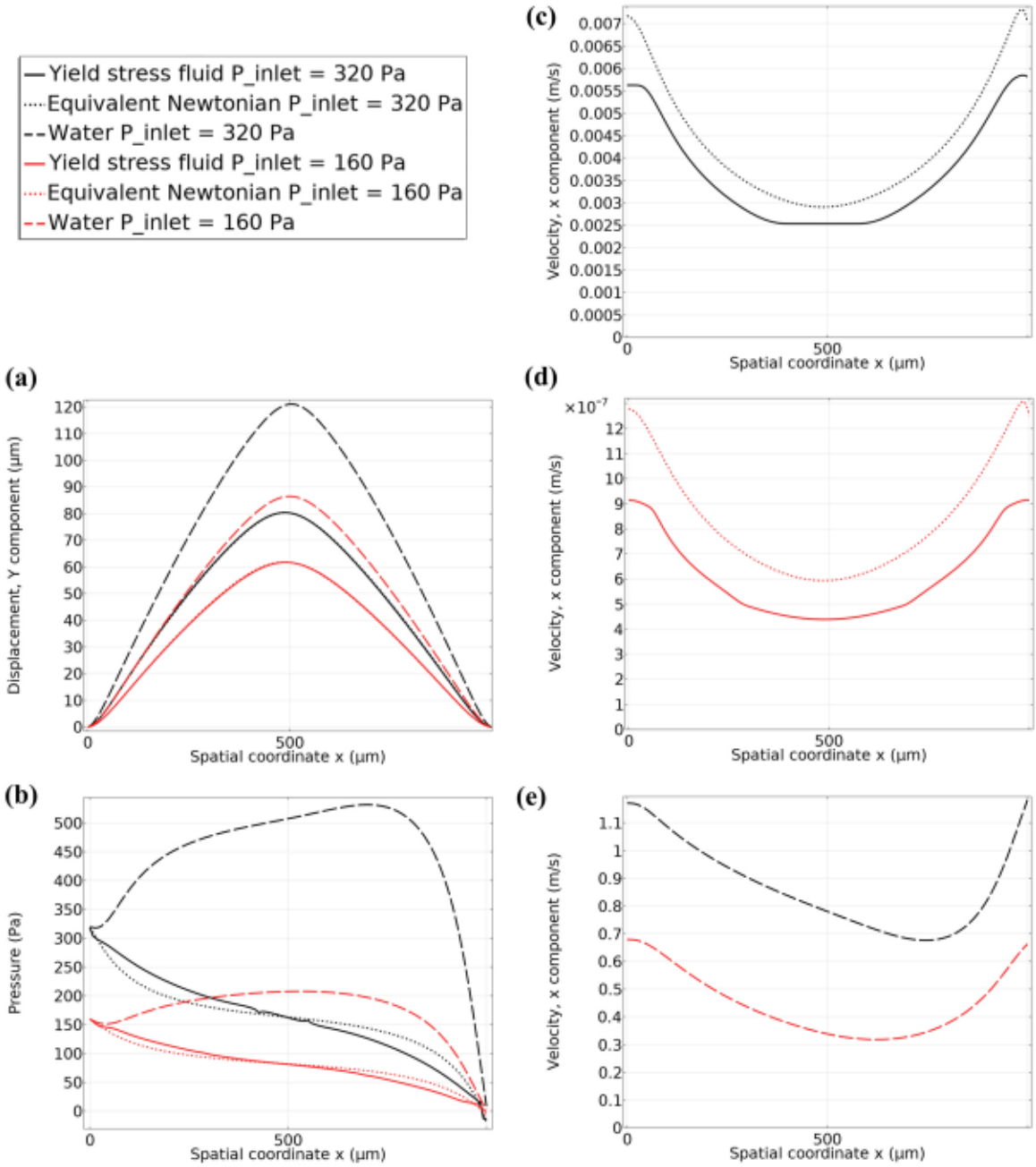

Fig. 3 – Displacement (a), pressure distribution along the x-direction (b) and horizontal velocity component distribution along the x-direction (c,d,e) in a rectangular duct of infinite depth, 1 millimeter length, 100 µm aperture and $E = 10^6$ Pa. Velocity and pressure distributions are given within the central plane. The cases corresponding to the yield stress fluid, the equivalent Newtonian fluid and water are represented by solid lines, dotted lines and dashed lines, respectively. Different colors represent different inlet pressures (in Pa): red for 160 Pa and black for 320 Pa.

simulation of Herschel-Bulkley fluids flow. In this regard, the individual flow rate in each element of the network might be determined from a relationship of the same type as Eq. (11). However, obtaining an analytical relationship between h_{eq} and ∇P remains a challenging task, as can be deduced from Fig. 4(b).

Fig. 5 presents the maximum wall displacement Y as a function of ∇P for the tested values of E. Both yield stress fluid and water cases are represented. It is worth noting that the maximum wall displacement for the equivalent Newtonian fluid is expected to be similar to the one of the yield stress fluid, as deduced from Fig. 3(a). This can be explained by the roughly identical pressure values obtained for the yield stress fluid and its Newtonian equivalent in the central zone in which the maximum displacement is attained (Fig. 3b). Therefore, it is the effective viscosity of the fluid in the channel rather than the distribution of local viscosities which determine the value of Y. Predictably, the maximum displacement increases when ∇P is increased for both the Newtonian and the Herschel-Bulkley fluids. It was observed that the dependence of Y on ∇P was well fitted by a power law of the type $Y = a\nabla P^b$ with b increasing and a decreasing as E increases (coefficient of determination $R^2 > 0.99$ in all cases). This is consistent with the fact that a should be equal

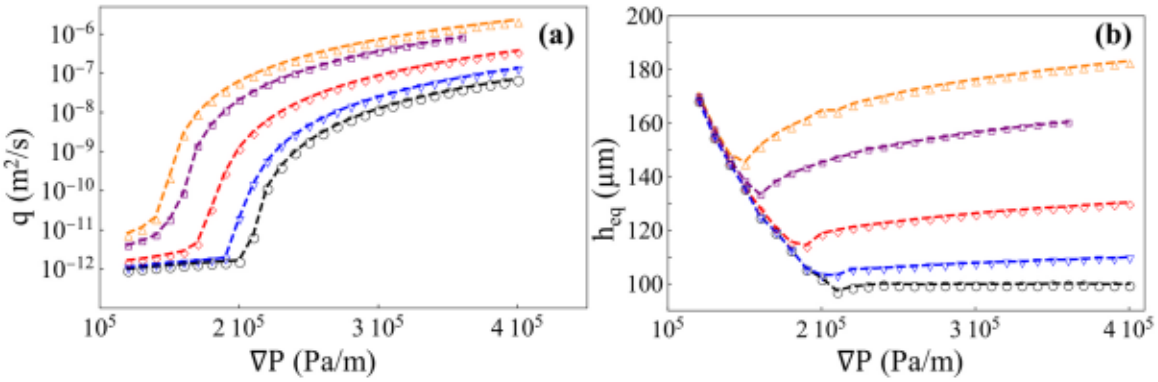

Fig. 4 – (a) q vs. ∇P relationships and (b) h_{eq} vs. ∇P relationships for the flow of the investigated yield stress fluid through a single rectangular duct of infinite depth, 1 millimeter length and 100 µm aperture. The results provided by the simulations are represented by symbols joined by dashed lines. The effect of Young's modulus E is represented with different colors and symbols: rigid duct (black circles), $E = 3 \times 10^5$ Pa (orange triangles), $E = 1 \times 10^6$ Pa (purple squares), $E = 1 \times 10^7$ Pa (red diamonds), $E = 1 \times 10^8$ Pa (blue inverted triangles).

to zero in the case of a rigid bundle (as E tends to infinity). The lower values of b obtained for the non-Newtonian fluid reveal that the channel deformation is more sensitive to ∇P in the case of a low-viscosity fluid as water. This may be a consequence of the transition from monotonic to non-monotonic pressure profile over the length direction observed for water as ∇P increased (Fig. 3b). Indeed, Y increases with increased ∇P not only as a consequence of the increase of the average pressure of the channel, but also as a consequence of the pressure in the central part of the channel becoming greater than P_{inlet}.

3.2.2. *Influence of inlet pressure and channel length on maximum wall displacement*

The relationship between Y and P_{inlet} is represented in Fig. S3 of the supplementary material. It should be mentioned that the series of data displayed in Fig. S3 were well fitted by an exponential function passing through (0,0). In a similar manner as in the previous figure, Y is an increasing function of P_{inlet} for both types of fluid. Y dependence on P_{inlet} was also well fitted by a power law of the type $Y = c\,\nabla P^d$ with c being lower for the higher values of h_i (coefficient of determination $R^2 > 0.99$ in all cases). While d decreased as h_i increased for the Herschel-Bulkley fluid, no significant dependence of d on h_i was evidenced for the two smaller values of h_i in the case of the Newtonian fluid.

Y was represented as a function P_{inlet} for different values of L in Fig. 6(a), showing increasing wall displacement as L increased. This is a consequence of the proximity of the constrained extremities when the channels are short, which limits the displacement of the solid wall to a greater extent as compared to longer channels. This results in higher local apertures and higher values of h_{eq} in the longest channels (Fig. 6b), i.e. for the lowest pressure gradients. Furthermore, ∇P dependence on q was fitted by the function $\nabla P = \nabla P_0 + eq^f$ ($f < 1$) for each value of L, resulting in good agreement. This fitting function had the same form as the fluid's constitutive equation and describes the stagnant state (q = 0) of the fluid below ∇P_0. It also accounts for the shear-thinning behavior of the fluid, as the increase in ∇P with increasing q is lower at the highest values of q due to the lower viscosity developed by the fluid. An apparent critical aperture can be defined as $h_0 = 2\tau_0/\nabla P_0$, which represents the size of a straight channel in which the onset of flow is produced at the same pressure gradient as the considered deformable channel. Fig. 6(c) shows that a yield stress can flow through a deformable channel of initial width h_0 under a pressure gradient inferior to $\nabla P_0 = 2\tau_0/h_0$, which is not possible in the case of a rigid

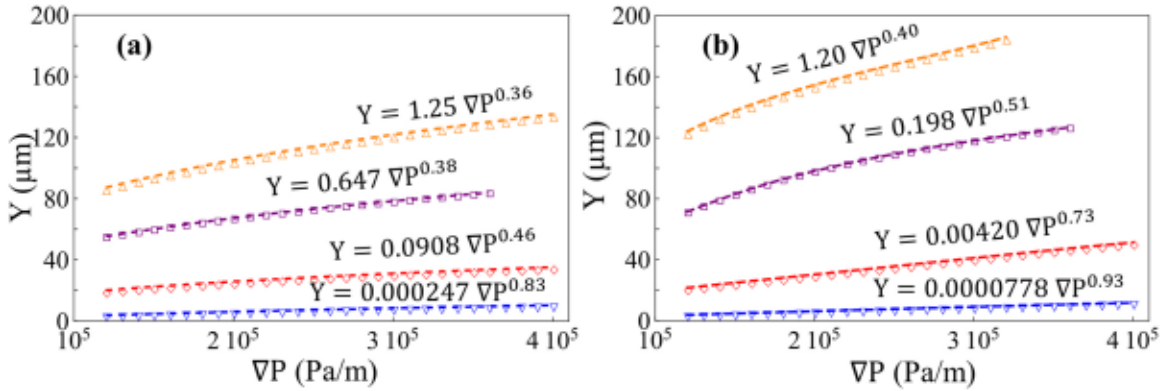

Fig. 5 – Maximum wall displacement Y vs. ∇P relationships for the flow of the investigated yield stress fluid (a) and water (b) through a single rectangular duct of infinite depth, 1 millimeter length and 100 µm aperture. The results provided by the simulations are represented by symbols joined by dashed lines. The effect of Young's modulus E is represented with different colors and symbols: rigid duct (black circles), $E = 3 \times 10^5$ Pa (orange triangles), $E = 1 \times 10^6$ Pa (purple squares), $E = 1 \times 10^7$ Pa (red diamonds), $E = 1 \times 10^8$ Pa (blue inverted triangles).

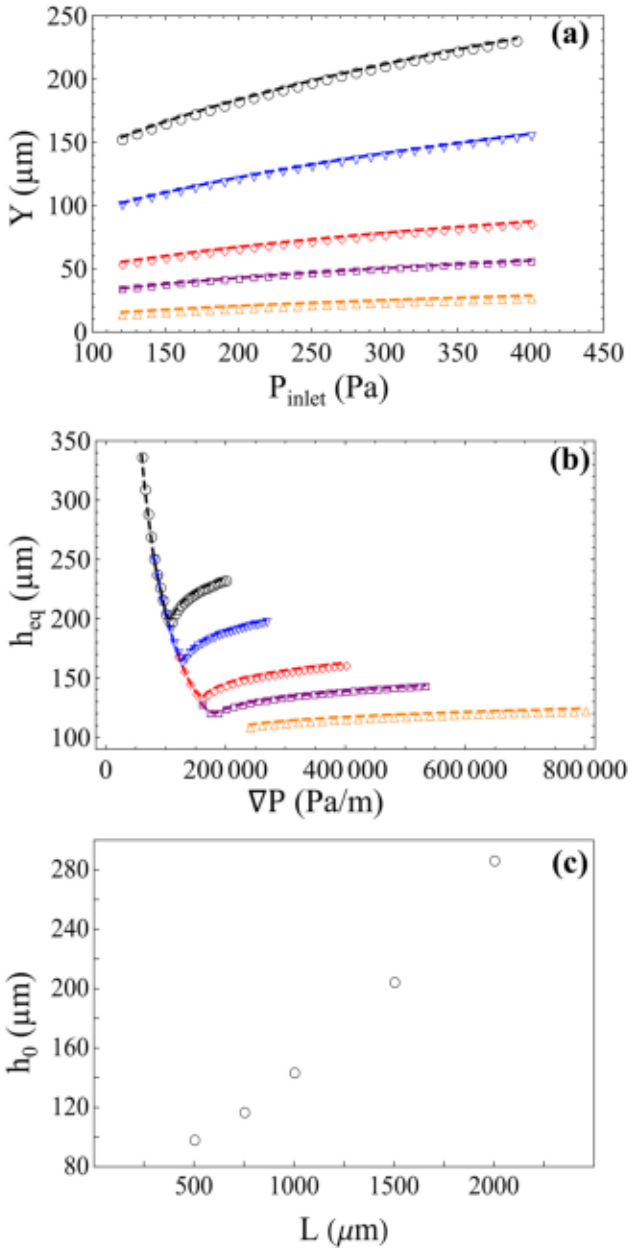

Fig. 6 – (a) Maximum wall displacement under different inlet pressures and (b) h_{eq} under different pressure gradients in a single rectangular duct of infinite depth and 100 μm aperture. The results for a set of channel lengths are represented: 2 mm (black circles), 1.5 mm (blue inverted triangles), 1 mm (red diamonds), 0.75 mm (purple squares) and 0.5 mm (orange triangles). E is equal to 10^6 Pa in all cases and the injection of the investigated yield stress fluid is considered. (c) h_0 as a function of L.

channel, as mentioned above. For example, h_0 is close to 200 μm for L = 1500 μm, which means that the onset of flow in the deformable channel is $\nabla P_0 = 2\tau_0/h_0$ = 100,000 Pa while the onset of flow in a rigid one would be $\nabla P_0 = 2\tau_0/h$ = 200,000 Pa. As can be obseved in Fig. 3(b), the local pressure gradient is much higher in the vicinity of the constrained extremities of a deformable duct than in the central part of the channel where the local apertures are higher due to deformation. In contrast, a constant high value of pressure gradient is obtained in a rigid channel over its whole length L. This explains that a lower length-averaged pressure gradient ∇P_0 is required to mobilize the yield stress fluid in a deformable channel.

An important point is that μ_{pm} is not a fluid property, as it also depends on the mechanical characteristics of the deformable porous medium. Indeed, the choice of using the permeability of the undeformed porous medium in Eq. (13) induces an extra decrease in μ_{pm} when u is increased with respect to the expected decrease in a rigid porous medium. This is illustrated by Fig. 7. Rigorously speaking, it is the permeability of the medium which is increased under higher values of u due to the higher levels of pressure deforming the solid. However, this increase in permeability depends in turn on the rheology of the fluid, given the coupling between the deformation of the solid and the rheology of the fluid. In other words, different rheological properties will result in different pressure distributions and wall shear stresses that will deform the solid to a different extent. Moreover, Fig. 7(b) shows that the value of α increases as u is increased above a threshold value (10^{-3} m/s in this case), contrarily to the case of the rigid bundle of channels.

3.3. *Transient flows of a yield stress fluids in deformable channels*

As mentioned in subsection 2.3.2, the time evolution of h_{eq} was computed for the 5 different aperture classes and for the 5 different values of $\bar{P}$, using T = 1 s. The obtained results were fitted to the following sinusoidal function using a standard least squares method:

$$h_{eq}(t) = \bar{h}\left(1 + a\sin\frac{2\pi}{T}(t - t_0)\right) \tag{19}$$

The average errors between the results provided by the fitting function and the numerical data were lower than 6% of $\bar{h}$ and 16% of a in all cases. The values of $\bar{h}$ and a obtained for the different aperture classes h_i are represented in Fig. S4 of the supplementary material for the highest and the lowest value $\bar{P}$. A linear relationship was obtained between $\bar{h}_i$ and h_i for every $\bar{P}$. The less accurate results were observed for the smaller ducts and the lower values of $\bar{P}$ ($\bar{P}$ = 250 Pa), as reflected by Fig. 8. The divergences observed for $\bar{P}$ = 250 Pa in Fig. 8 can be explained through comparison with the results obtained for steady flow. Indeed, it can be deduced from the red series displayed in Fig. 4(b) that h_{eq} depends significantly on ∇P for $\nabla P < 3.50 \times 10^5$ Pa, while h_{eq} attains a plateau value of ~ 125 μm for $\nabla P \geq 3.50 \times 10^5$ Pa. The oscillatory flow with $\bar{P}$ = 250 Pa covers the range of ∇P = (1.85×10^5, 3.09×10^5) Pa, which corresponds to the range of ∇P in which h_{eq} is not constant. This is not the case of the oscillatory flows with $\bar{P}$ = 1000 Pa, which cover the range of ∇P = (7.45×10^5, 1.24×10^6) Pa.

Q and μ_{pm} were represented are as a function of time for the oscillatory flow of a yield stress fluid through a bundle of straight rectangular ducts of infinite depth and 1 mm length in Fig. 9. The results for both the deformable and the rigid bundles are displayed. For all the investigated values of $\bar{P}$, $\mu_{pm}(t)$ was fitted through a standard least squares method to the following function:

$$\mu_{pm}(t) = \bar{\mu_{pm}}\left(1 + A\sin\frac{2\pi}{T}(t - t_1)\cos\frac{2\pi}{T}(t - t_2)\right) \tag{20}$$

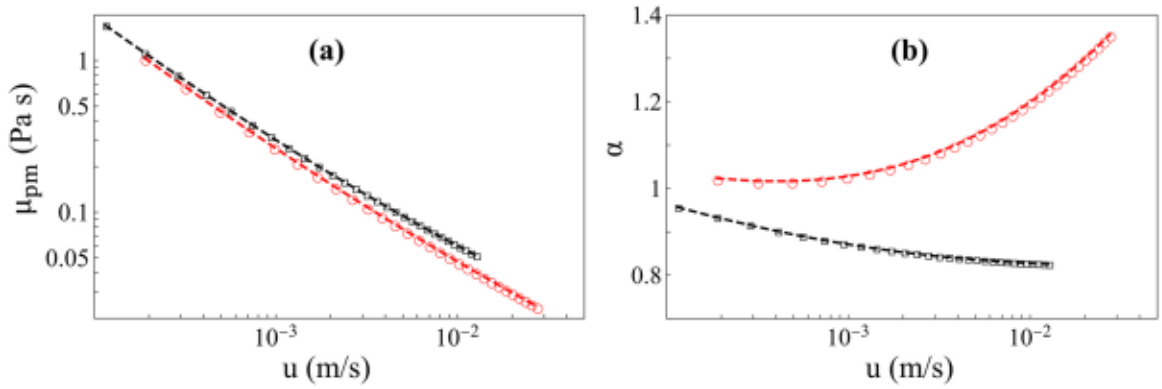

Fig. 7 – (a) Darcy viscosity μ_{pm} and (b) shift parameter α at for the injection of the yield stress fluid thorough a bundle of straight rectangular ducts of infinite depth and 1 mm length under different injection velocities. All the data points correspond to the steady state. The case of deformable ducts with $E = 10^6$ Pa is represented in red and the case of rigid ducts is represented in black for comparison purposes.

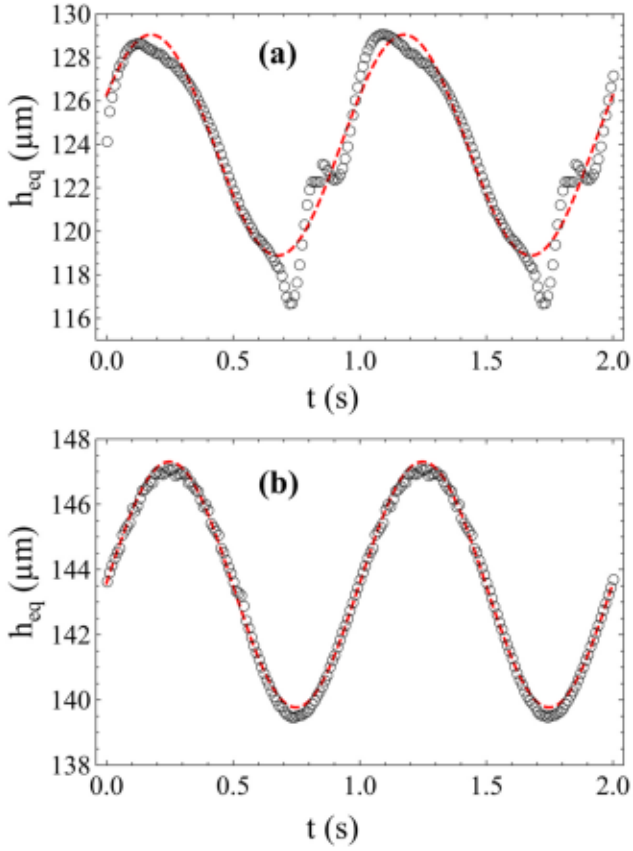

Fig. 8 – Evolution of equivalent aperture over time during oscillatory flow of the yield stress fluid through an elastic channel of 100 μm aperture, 1 mm length, infinite depth and $E = 10^7$ Pa. Two different average inlet pressures $\bar{P}$ are represented: (a) $\bar{P}$ = 250 Pa and (b) $\bar{P}$ = 1000 Pa. Circles represent the numerical results and dashed lines represent the proposed fit.

The values of t_1 and t_2 provided by the fitting procedure were close to – 0.66 s and – 0.086 s in all cases. However, μ_{pm}^{-} and A showed significant variation, as plotted in Fig. S5 of the supplementary material. Fig. 10 shows that the predictions made by the fitting function were in good agreement with the numerical μ_{pm} vs. t data in all cases, including Newtonian fluid flow.

Fig. 9 suggests proportionality between the macroscopic flow rates obtained in the elastic bundle $Q_{elastic}(t)$ and in the rigid bundle $Q_{rigid}(t)$, assuming a succession of steady states in the rigid bundle. This means that:

$$Q_{elastic}(t) = f(\bar{P})Q_{rigid}(t) \tag{21}$$

with $f(\bar{P})$ being the proportionality factor, and $Q_{rigid}(t)$ being calculated with Eq.(12). $f(\bar{P})$ was assumed to be constant for each value of $\bar{P}$, given that its standard deviation over time was lower than 4% in all cases for T = 1 s. Furthermore, $f(\bar{P})$ showed to be a linear function of $\bar{P}$ within the investigated range of $\bar{P}$. Indeed, the errors obtained with the fitting function $f(\bar{P}) = 1.11 + 3.71 \times 10^{-4}\,\bar{P}$ were lower than 0.7%. It should be noted that f(0) must be close to 1, given that the rigid and deformable channels behave almost identically when subjected to zero pressure (some variations may arise because of flow history). The previous equation allows for the prediction $Q_{elastic}(t)$ without any knowledge of the equivalent apertures $h_{eq}(t)$ of the deformed channels within the considered range of $\bar{P}$. To go further, an additional set of oscillatory flow simulations were performed with a fluid with $\tau_0 = 0$ Pa, k = 1 Pa s^n, n = 0.5 and μ_{max} = 10,000 Pa s (shear-thinning fluid without yield stress). The results of these additional simulations showed that Eq. (21), and the preceding analysis also applied to the case of power-law fluids without yield stress.

From the previous observations, it can be deduced that the relationship between the Darcy viscosity values obtained for the flow of the Herschel-Bulkley fluid through the elastic bundle, henceforth referred to as $\mu_{pm,elastic}(t)$, and the ones obtained for the flow through the rigid bundle (assuming a succession of steady states), henceforth referred to as $\mu_{pm,rigid}(t)$, is given by:

$$\mu_{pm,rigid}(t) = f(\bar{P})\mu_{pm,elastic}(t) \tag{22}$$

By using Eq.(13), $\mu_{pm,rigid}(t)$ can be written as:

$$\mu_{pm,rigid}(t) = \frac{\nabla P(t) K}{\frac{Q_{rigid}(t)}{W}} = \frac{\nabla P(t) K}{\frac{\sum_i n_i q(\nabla P(t), h_i)}{W}} \tag{23}$$

where $q(\nabla P_j, h_i)$ is given by Eq.(2).

Eqs.(22) and (23) provide a useful expression to predict $\mu_{pm,elastic}(t)$ in a simple manner:

$$\mu_{pm,elastic}(t) = \frac{\mu_{pm,rigid}(t)}{f(\bar{P})} = \frac{1}{f(\bar{P})} \frac{\nabla P(t) K}{\frac{\sum_i n_i q(\nabla P(t), h_i)}{W}} \tag{24}$$

One may argue that Eqs.(22) and (24) should only apply to slowly oscillating flows, given the quasi-stationary

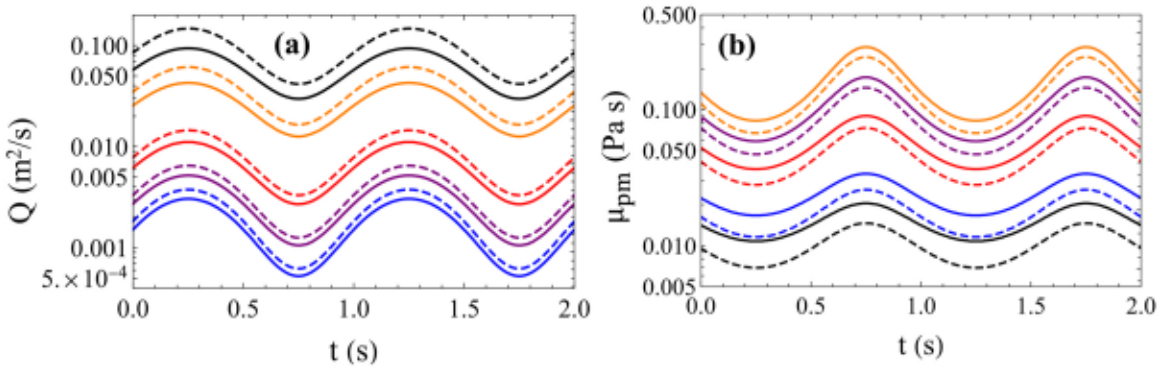

Fig. 9 – (a) Flow rate per unit depth Q and (b) Darcy viscosity μ_{pm} as a function of time for the oscillatory flow of a yield stress fluid through a bundle of straight rectangular ducts of infinite depth and 1 mm length. Dashed lines correspond to deformable ducts with $E = 10^7$ Pa and solid lines correspond to rigid ducts. Different colors represent different average inlet pressures: 250 Pa (blue), 300 Pa (purple), 400 Pa (red), 700 Pa (orange), 1000 Pa (black).

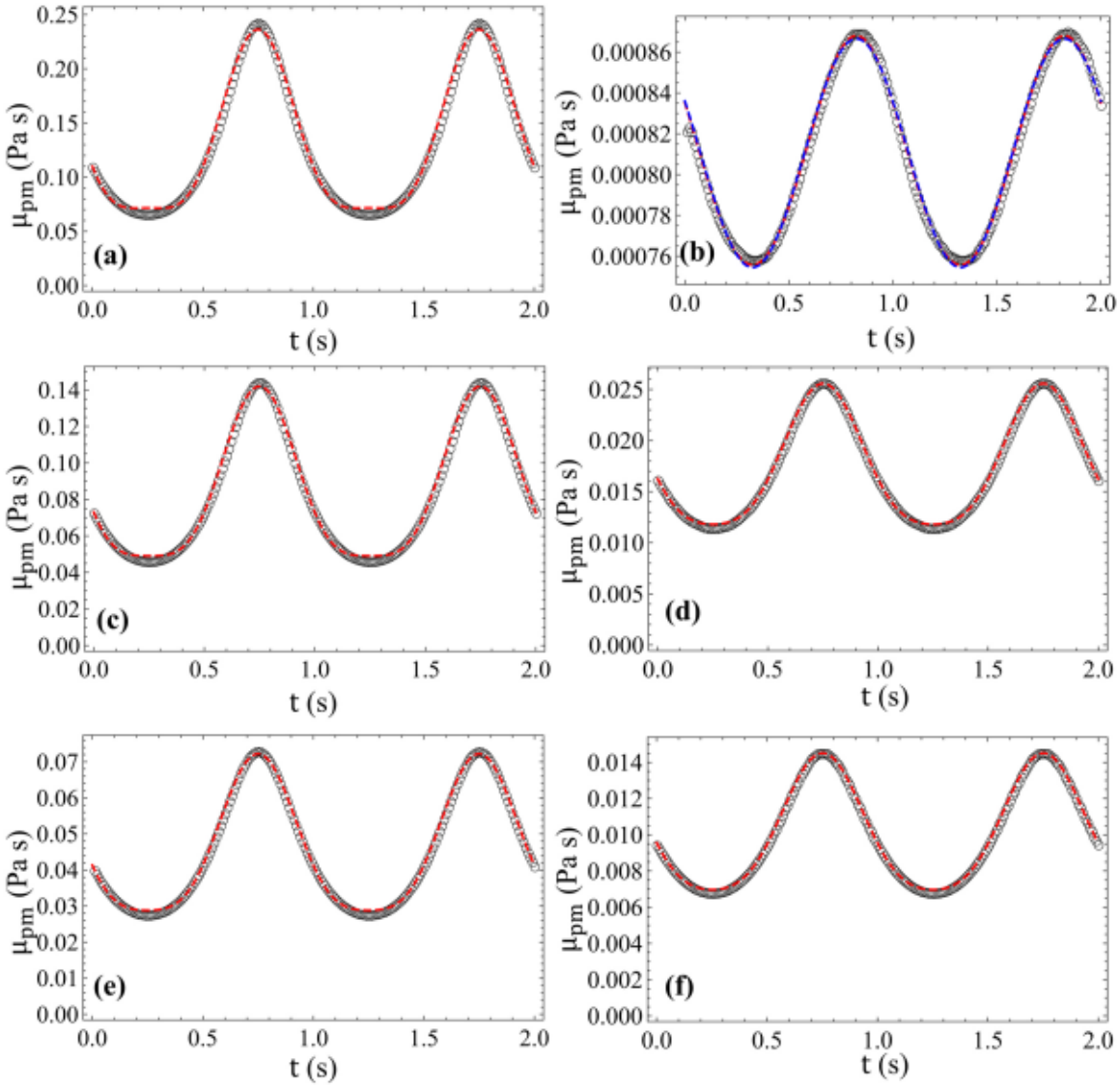

Fig. 10 – Predictions of $\mu_{pm,elastic}(t)$ obtained using the fitting function (red dashed lines) vs. numerical results (black symbols): (a) 250 Pa (c) 300 Pa (d) 700 Pa (e) 400 Pa and (f) 1000 Pa. (b) corresponds to water at 250 Pa.

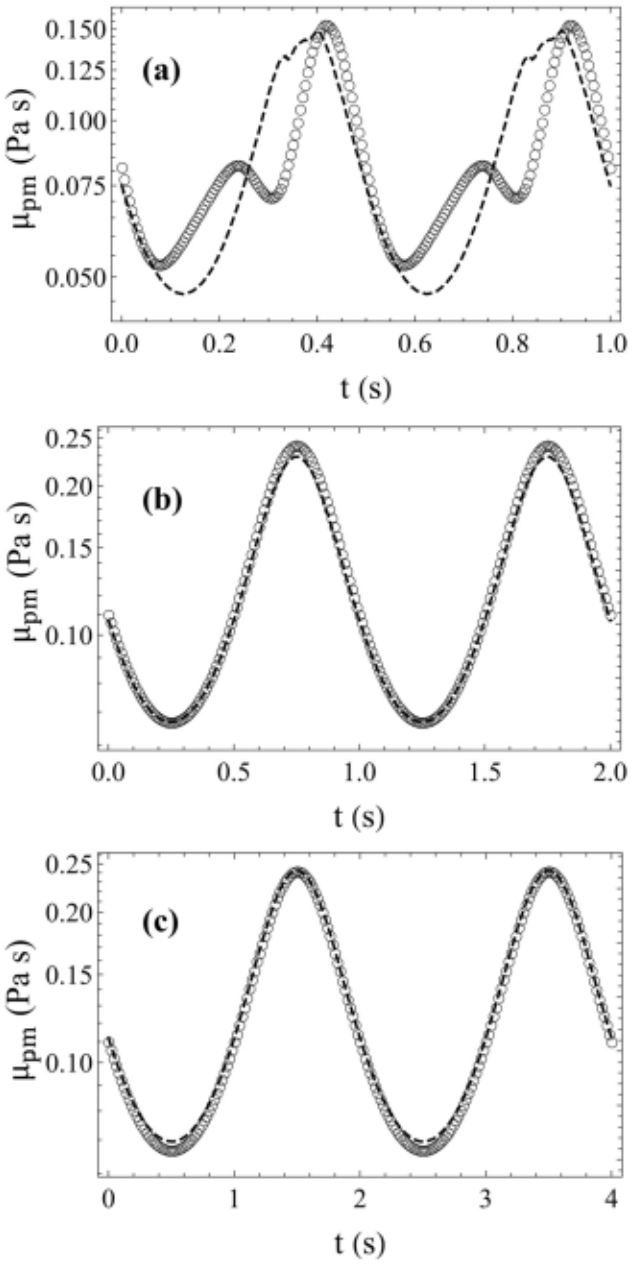

Fig. 11 – Predictions of $\mu_{pm,elastic}(t)$ by assuming proportionality between $Q_{elastic}(t)$ and $Q_{rigid}(t)$ (dashed lines) vs. numerical results (black symbols) for $\bar{P}$ = 250 Pa. (a) T = 0.5 s, (b) T = 1 s, (c) T = 2 s. The predictions of $\mu_{pm,elastic}(t)$ were obtained by multiplying $\mu_{pm,rigid}(t)$ by the time averaged value of $\frac{\mu_{pm,elastic,simulated}(t)}{\mu_{pm,rigid}(t)}$ in each case, $\mu_{pm,elastic,simulated}(t)$ being the value of $\mu_{pm,elastic}(t)$ provided by the DNS.

assumption used for the calculation of $Q_{rigid}(t)$. In order to assess the range of validity of these equations, supplementary numerical simulations were performed in the investigated porous media using T = 0.5 s and T = 2 s while keeping $\bar{P}$ = 250 Pa. The values of the standard deviation of $f(\bar{P})$ over time reported by such simulations were 28.8% for T = 0.5 s and 1.34% for T = 2 s. To illustrate the accuracy of the predictions made by Eq. (24), Fig. 11 shows the predictions of $\mu_{pm,elastic}(t)$ obtained assuming proportionality between $Q_{elastic}(t)$ and $Q_{rigid}(t)$, depending on T. Good accuracy is obtained for T > 0.5, which is consistent with the preceding remarks.

4. Conclusion

Pioneer numerical simulations of the flow of yield stress fluids through a deformable porous medium have been conducted by using an Arbitrary Lagrangian-Eulerian technique. The main assumptions are the linear elasticity of the solid and the use of a bundle-of-channels model to represent the geometry of the pores. Both stationary and oscillatory flow have been considered. Furthermore, a simple model to predict these flows at the Darcy scale has been developed based on the current numerical results.

The main conclusions may be summarized as follows:

- Yield stress fluids show a more homogeneous velocity distribution in deformable channels than their Newtonian equivalents, while maximum wall displacement remains unaffected. A power-law dependence has been observed between the maximum solid displacement and ∇P, with an exponent which decreases as Young's modulus is increased.
- The threshold pressure gradient for the flow of a yield stress fluid through a deformable channel is significantly lower than the one for a rigid channel.
- The relationship between the total flow rate and the pressure gradient through the porous medium during stationary flow was analogous to the fluid's constitutive equation.
- Darcy viscosity decreases with increasing injection pressure in the deformable porous medium with respect to the rigid one, resulting from the associated increase in permeability.
- The value of the shift factor between bulk and Darcy viscosity increases as Darcy velocity is increased above a critical value, contrarily to the case of the rigid bundle of channels.

Regarding transient flows:

- The time evolution of equivalent channel apertures and Darcy velocity were shown to fit well to a sinusoidal function.
- An equation has been proposed allowing for the prediction of the flow rate obtained during oscillatory flow without any knowledge of the equivalent apertures of the individual deformed channels, and the conditions of its validity have been examined.

Analytical relationships between h_{eq} and ∇P for any value of the inlet pressure must still be obtained. Nevertheless, the current work shows that knowledge of such relationships is not necessary in all cases. Indeed, the total flow rate through the elastic bundle of channels has been shown to be proportional to the one obtained for the elastic bundle within the range of investigated boundary conditions. These results represent a valuable starting point for the development of a deformable pore network model. In parallel, the development of a macroscopic transport model should be addressed by using homogenization techniques applied to the local problem.

Declaration of Competing Interest

The authors declare that they have no known competing financial interests or personal relationships that could have appeared to influence the work reported in this paper.

Appendix A. Supporting information

Supplementary data associated with this article can be found in the online version at doi:10.1016/j.cherd.2023.03.004.

References

Abbas Nejad, A., Talebi, Z., Cheraghali, D., Shahbani-Zhhiri, A., Norouzi, M., 2018. Pulsatile flow of non-Newtonian blood fluid inside stenosed arteries: Investigating the effects of viscoelastic and elastic walls, arteriosclerosis, and polycythemia diseases. Comput. Methods Prog. Biomed. 154, 109–122.

Alves, R.J., Magalhaes, M.D.C., Carrasco, E.V.M., 2013. Determination of the transverse Young's modulus (TYM) of wood by means of an input power technique. Constr. Build. Mater. 42, 11–21.

Anand, V., Christov, I.C., 2021. Revisiting steady viscous flow of a generalized newtonian fluid through a slender elastic tube using shell theory. ZAMM - J. Appl. Math. Mech. Z. Für Angew. Math. Und Mech. 101 (2), e201900309.

Anand, V., David Jr., J., Christov, I.C., 2019. Non-newtonian fluid–structure interactions: static response of a microchannel due to internal flow of a power-law fluid. J. Non-Newton. Fluid Mech. 264, 62–72.

Bauer, D., Talon, L., Peysson, Y., Ly, H.B., Bâtot, G., Chevalier, T., Fleury, M., 2019. Experimental and numerical determination of Darcy's law for yield stress fluids in porous media. Phys. Rev. Fluids 4, 063301.

Bear, Jacob, 1972. Dynamics of Fluids in Porous Media, Dover. ISBN 0–486-65675–6.

Bergamasco, L., Izquierdo, S., Pagonabagarra, I., Fueyo, N., 2015. Multi-scale permeability of deformable fibrous porous media. Chem. Eng. Sci. 126, 471–482.

Boyko, E., Christov, I.C., 2023. Non-Newtonian fluid–structure interaction: flow of a viscoelastic Oldroyd-B fluid in a deformable channel. J. Non-Newton. Fluid Mech. 313, 104990.

Boyko, E., Bercovici, M., Gat, A.D., 2017. Viscous-elastic dynamics of power-law fluids within an elastic cylinder. Phys. Rev. Fluids 2, 073301.

Canic, S., Lamponi, D., Mikelic, A., Tambaca, J., 2005. Self-consistent effective equations modeling blood flow in medium-to-large compliant arteries. Multiscale Model. Simul. 3, 559–596.

Chakraborty, D., Prakash, J.R., 2015. Viscoelastic fluid flow in a 2D channel bounded above by a deformable finite-thickness elastic wall. J. Non-Newton. Fluid Mech. 218, 83–98.

Chauveteau, G., 1982. Rodlike polymer solution flow through fine pores: influence of pore size on rheological behavior. J. Rheol. 26, 111.

Chauveteau, G., Zaitoun, A.: Basic rheological behavior of xanthan polysaccharide solutions in porous media: effects of pore size and polymer concentration. In: European Symposium on Enhanced Oil Recovery, Bournemouth, England (1981).

Chhabra, R.P., Richardson, J.F., 2008. Non-Newtonian flow and applied rheology: engineering applications. Butterworth-Heinemann/Elsevier, Amsterdam; Boston.

Chien, S., 1970. Shear dependence of effective cell volume as a determinant of blood viscosity. Science 168 (3934), 977–979.

Comba, S., Dalmazzo, D., Santagata, E., Sethi, R., 2011. Rheological characterization of xanthan suspensions of nanoscale iron for injection in porous media. J. Hazard. Mater. 185, 598–605.

COMSOL Multiphysics Version 5.3. COMSOL AB, Stockholm, Sweden. ⟨www.comsol.com⟩ (2017).

Di Federico, V., 1997. Estimates of equivalent aperture for Non-Newtonian flow in a rough-walled fracture. Int. J. Rock. Mech. Min. Sci. 34 (7), 1133–1137.

Di Federico, V., 1998. Non-Newtonian flow in a variable aperture fracture. Transp. Porous Media 30 (1), 75–86.

Ferrás, L.L., Nóbrega, J.M., Pinho, F.T., 2012. Analytical solutions for Newtonian and inelastic non-Newtonian flows with wall slip. J. Non-Newton. Fluid Mech. 175–176, 76–88.

Forchheimer, P., 1901. Wasserberwegng durch Boden. Forschtlft ver D. Ing. 45 (50), 1782–1788.

Fung, Y.C., 2013. Biomechanics: Mechanical Properties of Living Tissues. Springer Science & Business Media.

Gomez, Michael, Moulton, Derek E., Vella, Dominic, 2017. Passive control of viscous flow via elastic snap-through. Phys. Rev. Lett. 119 (14), 144502.

Grotberg, J.B., 1994. Pulmonary flow and transport phenomena. Annu. Rev. Fluid Mech. 26, 529–571.

Grotberg, J.B., Jensen, O.E., 2004. Biofluid mechanics in flexible tubes. Annu. Rev. Fluid Mech. 36, 121–147.

Heil, M., Hazel, A.L., 2011. Fluid-structure interaction in internal physiological flows. Annu. Rev. Fluid Mech. 43, 141–162.

M.D.M. Innocentini; R.K. Faleiros; R. Pisani; I. Thijs; J. Luyten; S. Mullens. Permeability of porous gelcast scaffolds for bone tissue engineering., 17(5), 615–627 (2010).

Kim, Jun-Mo, Parizek, R.R., 2005. Numerical simulation of the Rhade effect in layered aquifer systems due to groundwater pumping shutoff. Adv. Water Resour. 28, 627–642.

Kizilova, N., Hamadiche, M., Hak, G.-eM., 2012. Mathematical models of biofluid flows in compliant ducts. Arch. Mech. 64, 65–94.

Kovscek, A.R., Bertin, H.J., 2003. Foam mobility in heterogeneous porous media. Transp. Porous Media 52, 17–35.

Lavrov, A. Non-Newtonian fluid flow in rough-walled fractures: A brief review, in Proceedings of ISRM SINOROCK 2013, 18–20 June, Shanghai, China Int. Soc. for Rock Mech., Lisboa, Portugal (2013).

Ling, Y., Tang, J., Liu, H., 2021. Numerical investigation of two-phase non-Newtonian blood flow in bifurcate pulmonary arteries with a flow resistant using Eulerian multiphase model. Chem. Eng. Sci. 233, 116426.

Longpré-Girard, M., Martel, R., Robert, T., Lefebvre, R., Lauzon, J.-M., 2016. 2D sandbox experiments of surfactant foams for mobility control and enhanced LNAPL recovery in layered soils. J. Contam. Hydrol. 193, 63–73.

Lopes, D., Puga, H., Teixeira, J., Lima, R., 2020. Blood flow simulations in patient-specific geometries of the carotid artery: a systematic review. J. Biomech. 111, 110019 (2020).

López, X., Valvatne, P.H., Blunt, M.J., 2003. Predictive network modeling of single-phase non-Newtonian flow in porous media. J. Colloid Interface Sci. 264 (1), 256–265.

McDonald, J.C., Whitesides, G.M., 2002. Poly(dimethylsiloxane) as a material for fabricating microfluidic devices. Acc. Chem. Res. 35, 491–499.

Morgan, P., Parker, K.H., 1989. A mathematical model of flow through a collapsible tube-I. Model and steady flow results. J. Biomech. 22, 1263–1270.

Omirbekov, S., Davarzani, H., Colombano, S., Ahmadi-Senichault, A., 2020. Experimental and numerical upscaling of foam flow in highly permeable porous media. Adv. Water Resour. 146, 103761.

Pedley, T.J., 1980. The Fluid Mechanics of Large Blood Vessels. Cambridge University Press, Cambridge.

Peyrounette, M., Davit, Y., Quintard, M., Lorthois, S., 2018. Multiscale modelling of blood flow in cerebral microcirculation: Details at capillary scale control accuracy at the level of the cortex. PLoS One 13 (1), e0189474.

Pipe, C.J., Majmudar, T.S., McKinley, G.H., 2008. High shear rate viscometry. Rheol. Acta 47, 621–642.

Pourjafar, M., Sadeghy, K., 2017. Pressure-driven flows of quemada fluids in a channel lined with a poroelastic layer: a linear stability analysis. J. Non-Newton. Fluid Mech. 242, 23–47.

Quintard, M., Whitaker, S., 1993. Transport in ordered and disordered porous media: Volume averaged equations, closure problems, and comparison with experiment. Chem. Eng. Sci. 48, 2537–2564.
Raj, A., Sen, A.K., 2016. Flow-induced deformation of compliant microchannels and its effect on pressure–flow characteristics. Microfluid. Nanofluids 20, 31.
Raj, M.K., Chakraborty, J., DasGupta, S., Chakraborty, S., 2018. Flow-induced deformation in a microchannel with a non-Newtonian fluid. Biomicrofluidics 12, 034116.
Rodríguezde Castro, A., 2019. Extending Darcy's law to the flow of Yield Stress fluids in packed beads: method and experiments. Adv. Water Resour. 126, 55–64.
Rodríguezde Castro, A., Agnaou, A., 2019. Numerical investigation of the apparent viscosity dependence on darcy velocity during the flow of shear-thinning fluids in porous media. Transp. Porous Media.
Rodríguezde Castro, A., Goyeau, B., 2021. A pore network modelling approach to investigate the interplay between local and Darcy viscosities during the flow of shear-thinning fluids in porous media. J. Colloid Interface Sci. 590, 446–457.
Rodríguezde Castro, A., Radilla, G., 2016. Non-Darcian flow experiments of shear-thinning fluids through rough-walled rock fractures. Water Resour. Res. 52, 9020–9035.
Rodríguezde Castro, A., Radilla, G., 2017a. Non-Darcian flow of shear-thinning fluids through packed beads: experiments and predictions using Forchheimer's law and Ergun's equation. Adv. Water Resour. 100, 35–47.
Rodríguezde Castro, A., Radilla, G., 2017b. Flow of yield and Carreau fluids through rough-walled rock fractures: prediction and experiments. Water Resour. Res 53 (7), 6197–6217.
Rodríguezde Castro, A., Ahmadi-Sénichault, A., Omari, A., 2021. Analysis of the length scale characterized by the Yield Stress fluids porosimetry Method for consolidated media: comparison with Pore Network Models and Mercury Intrusion Porosimetry. Hydrogeol. J. 289, 2853–2866.
Rosti, Marco Edoardo, Pramanik, Satyajit, Brandt, Luca, Mitra, Dhrubaditya, 2020. The breakdown of Darcy's law in a soft porous material. Soft Matter 10, 939–944.
Sankar, D.S., Hemalatha, K., 2007. Pulsatile flow of Herschel–Bulkley fluid through catheterized arteries – a mathematical model. Appl. Math. Model. 31, 1497–1517.
Sankar, D.S., Lee, U., 2009. Mathematical modeling of pulsatile flow of non-Newtonian fluid in stenosed arteries. Commun. Nonlinear Sci. Numer. Simul. 2971–2981.
Savins, J.G., 1969. Non-Newtonian flow through porous media. Ind. Eng. Chem. 61, 18–47.
Scott Blair, G.W., Spanner, D.C., 1974. An introduction to biorheology. Elsevier Scientific Publishing Company, Amsterdam, Oxford and New York.
Shende, T., Niasar, V., Babaei, M., 2021. Upscaling non-Newtonian rheological fluid properties from pore-scale to Darcy's scale. Chem. Eng. Sci., 116638.
Sheng, J.J., 2011. Modern chemical enhanced oil recovery, theory and practice. Elsevier, Boston.
Skelland, A.H.P., 1967. Non-Newtonian Flow and Heat Transfer. Wiley, New York.
Sochi, T., 2010. Modelling the flow of yield-stress fluids in porous media. Transp. Porous Media 85, 489–503.
Sorbie, K.S., Clifford, P.J., Jones, R.W., 1989. The rheology of pseudoplastic fluids in porous media using network modeling. J. Colloid Interface Sci. 130, 508–534.
Talon, L., Bauer, D., 2013. On the determination of a generalized Darcy equation for yield-stress fluid in porous media using a lattice-Boltzmann TRT scheme. Eur. Phys. J. E 36, 139.
Tosco, T., Marchisio, D.L., Lince, F., Sethi, R., 2013. Extension of the Darcy-Forchheimer law for shear-thinning fluids and validation via pore-scale flow simulations. Transp. Porous Media 96, 1–20.
Van de Vosse, F.N., 2013. Cardiovascular Fluid Mechanics - lecture notes 8W090 -. Eindhoven University of Technology department of Biomedical Engineering.
Vedeneev, V., 2020. Nonlinear steady states of hyperelastic membrane tubes conveying a viscous non-Newtonian fluid. J. Fluids Struct. 98, 103113.
Venkatesh, A., Anand, V., Narsimhan, V., 2022. Peeling of linearly elastic sheets using complex fluids at low Reynolds numbers. J. Non-Newton. Fluid Mech. 309, 104916.
Whitaker, R.J., Heil, M., Jensen, O.E., Walters, S.L., 2010. Predicting the onset of high-frequency self-excited oscillations in elastic-walled tubes. Proc. R. Soc. A 466, 3635–3657.
Whitaker, S., 1999. The Method of Volume Averaging. Kluwer Academic Publishers, Dordrecht.